Medium-density amorphous ice

Alexander Rosu-Finsen[1], Michael B. Davies[2,3], Alfred Amon[1], Han Wu,[4] Andrea Sella[1], Angelos Michaelides[3,2]*, Christoph G. Salzmann[1]*

Affiliations:

[1] Department of Chemistry, University College London; London, WC1H 0AJ, United Kingdom.

[2] Department of Physics and Astronomy, University College London; London, WC1E 6BT, United Kingdom.

[3] Yusuf Hamied Department of Chemistry, University of Cambridge; Cambridge, CB2 1EW, United Kingdom.

[4] Department of Chemical Engineering, University College London; London, WC1E 7JE, United Kingdom.

*Corresponding authors. Email: c.salzmann@ucl.ac.uk, am452@cam.ac.uk

Abstract:

Amorphous ices govern a range of cosmological processes and are potentially key materials for explaining the anomalies of liquid water. A substantial density gap between low-density amorphous (LDA) and the high-density amorphous ices (HDA) with liquid water in the middle is a cornerstone of our current understanding of water. However, we show that ball milling 'ordinary' ice I*h* at low temperature gives a structurally distinct medium-density amorphous ice (MDA) within this density gap. These results raise the possibility that MDA is the true glassy state of liquid water or alternatively a heavily sheared crystalline state. Remarkably, the compression of MDA at low temperature leads to a sharp increase of its recrystallization enthalpy highlighting that H_2O can be a high-energy geophysical material.

One-Sentence Summary: Shaken, not stirred: Ball milling gives amorphous ice in the density range of liquid water.

Main Text:

Water has a remarkably rich and fascinating phase diagram with 20 crystalline phases and at least two families of amorphous forms(*1-7*). While three new crystalline phases have been discovered in the last five years alone(*2-6*), the discovery of amorphous states is much less common. The current complement of amorphous forms comprises low-density amorphous ice (LDA), first made through vapor deposition in the 1930s(*8*). By compression of ice I*h* or LDA at low temperatures, high-density amorphous ice (HDA) was made in the 1980s(*9, 10*). Heating HDA under pressure gives either expanded high-density (eHDA) or very high-density amorphous ice (vHDA), as reported in the early years of this century(*11, 12*). As their names suggest, amorphous ices are distinguished principally by their densities, with LDA having a density of 0.94 g cm^{-3} and the HDAs starting from 1.13 g cm^{-3} at ambient pressure and 77 K(*7*). This leaves a conspicuous gap in densities around the density of liquid water (1 g cm^{-3}) which is not filled by any known crystalline phases and it is unclear if homogeneous amorphous ice can display a density in this gap(*13-15*). This gap and the question if the amorphous ices have corresponding liquid states below a liquid-liquid critical point is a topic of great interest with respect to explaining water's many anomalies(*16-26*). The fact that amorphous ice is the most common form of ice in the Universe(*27*) underpins the need to understand the structurally disordered states of H_2O.

Aside from the previously reported techniques for making amorphous ices, ball milling is an established technique for making amorphous materials in general(*28*). The method is widely used for metallic alloys, inorganic compounds and pharmaceuticals(*28-30*) but has not been applied to ice. At the heart of the amorphization processes are ball-crystal-ball impact events that exert a combination of compressive and shear forces on the crystalline starting materials (Fig. 1A). While local melting effects have been discussed as the origin for amorphization, the introduction of dislocation defects seems to be the main driving force(*31*). In general, the amorphization through ball milling is most effective at low temperatures(*32*).

We show that low-temperature ball milling of ice I*h* leads to amorphous ice with a density in the gap between LDA and HDA. We cooled a grinding jar to 77 K with liquid nitrogen, filled it with ice and stainless-steel balls, and firmly closed it (Fig. 1B). To achieve the amorphization, the entire assembly was shaken vigorously for a range of ball-milling cycles(*33*).

We see the formation of amorphous ice after 80 ball-milling cycles from the broad X-ray diffraction features with peak maxima at 1.93 and 3.04 $Å^{-1}$ (Fig. 1C). The shift of the first strong diffraction peak (FSDP) at 1.93 $Å^{-1}$ away from the most intense Bragg peaks of ice I*h* signifies major structural changes. For comparison, cryogenic ball milling of the isostructural NH_4F I*h* results in the broadening without shifting of the Bragg peaks indicating only a reduction of the crystallite sizes (Fig. S1). Ball milling the ice II, IX and V high-pressure phases does also not yield any amorphous materials (Fig. S2) suggesting that the low-density ice I*h* crystal structure is particularly susceptible towards amorphization. Similar observations of ice I*h* occur in the context of pressure-induced amorphization to HDA(*9*).

A comparison with the diffraction patterns of other amorphous ices highlights that the amorphous ice obtained through ball milling is structurally unique (Fig. S3). The closest match in terms of peak positions is HDA. In contrast to HDA(*10*), the ball-milled amorphous ice does not transform to LDA upon heating at ambient pressure (Fig. 1C). Instead, the diffraction patterns collected upon heating show recrystallization to stacking disordered ice I

(ice I*sd*) above ~140 K which later transforms to the stable ice I*h*. We performed a quantitative analysis of the cubic/hexagonal stacking disorder in the ice I*sd* using the MCDIFFaX software(*34*) (Fig. S4). The ice I*sd* we obtained from heating the ball-milled ice contains 31% cubic stacking. The amorphous ice does not recrystallize to the fully hexagonal ice I*h* starting material, which underpins substantial structural changes upon amorphization.

We monitored the progress of the ball milling quantitatively with differential scanning calorimetry (DSC) (Fig. 1D). The recrystallization of the amorphous ice manifests as an exothermic phase transition at ~150 K which increases in area with increasing milling cycles. We obtained an enthalpy of –1.16 ± 0.09 kJ mol^{-1} (SD, *N*=3) after 40 milling cycles. Further increase to 80 milling cycles gives a heat release of –1.21 ± 0.15 kJ mol^{-1} (SD, *N*=3) indicating that the amorphization process is close to completion after 40 milling cycles. The areas of the exotherms are independent of the diameters of the stainless-steel balls in the 10 to 20 mm range (Fig. S5) illustrating that the amorphization process takes place robustly within a range of different ball-milling conditions. Stainless-steel balls give the best results in terms of amorphization compared to Teflon-coated or hardened-steel balls (Fig. S6).

The progressive amorphization upon balling milling was also followed quantitatively by fully crystallizing the amorphous samples through heating and analyzing the changes in the intensities of the ice I*h* Bragg peaks (Fig. S7). Consistent with the increases in the areas of the exotherms (Fig. 1D), the percentages of the amorphous content from the X-ray diffraction analysis increase steadily up to 40 milling cycles and then level off at around 70% (Fig. 1E).

Analysis of the half-widths of the ice I*h* Bragg peaks shows no systematic change in particle size of the ice I*h* contaminant as its amount decreases during the ball milling (Fig. S8). Optical microscopy of the ball-milled sample after 80 milling cycles shows mainly a disordered, opaque material consistent with an amorphous material (Fig. 1F). A minor fraction of transparent particles with some sharp edges, and hence likely crystalline ice I*h*, were also observed (Fig. 1F, arrows). The overall appearance of the ball-milled ice is that of large chunks consisting of a densely compacted powder. Inevitably, as more amorphous ice forms, a small fraction of the ice I*h* crystals will become increasingly shielded from the effects of ball milling. A small contribution from vapor condensation towards the ice I*h* content during the X-ray diffraction analysis cannot be excluded. The possibility that the incomplete amorphization is due to recrystallization caused by local heating effects during the ball milling seems unlikely because the crystalline contaminant is ice I*h* and not ice I*sd* to which the amorphous material recrystallizes upon heating (Fig. S4).

We collected Raman spectra of a ball-milled sample in the spectral range of the O-H stretching modes (Fig. 1G). While the X-ray diffraction data was closest to HDA, the Raman spectrum of the ball-milled ice is closer to LDA than to HDA. Consistent with the earlier X-ray diffraction analysis, we show that a maximal contribution of ~30% ice I*h* can be subtracted from the spectrum before the baseline below 3000 cm^{-1} begins to display an unphysical negative slope (Fig. S9). The main effect of the subtraction is a decrease in relative intensity of the most intense peak which shifts slightly by 4 cm^{-1} to 3100 cm^{-1}.

We determined the bulk densities of ball-milled samples using buoyancy measurements in liquid nitrogen. The samples become denser as the amorphization progresses closely following the trend of the amorphous content (Fig. 1E). After 80 milling cycles, the ball-milled ice has a density of 1.02 ± 0.03 g cm^{-3} (SD, *N*=3) at 77 K. Since the

sample is 69 ± 5% (SD, *N*=3) amorphous, it follows that the amorphous fraction has a density of 1.06 ± 0.06 g cm^{-3} (SD, *N*=3). This density falls into the gap between LDA (0.94 g cm^{-3}) and HDA (1.15 g cm^{-3})(*10, 12*). We therefore name the amorphous ice obtained from ball milling medium-density amorphous ice (MDA).

A continuous shift of the FSDP to lower *Q* values was previously observed during the HDA to LDA transition upon heating at ambient pressure(*13, 35*). In contrast, the transitions of eHDA and vHDA to LDA appear to be sharper(*14, 35, 36*). The question arises whether MDA is equivalent to a HDA→LDA transition state. A major argument against this is that the transition states all transform to LDA upon heating whereas MDA transforms to ice I*sd* at ~20 K higher temperature. The transition state at 114 K in the X-ray diffraction data(*36*) shows the best fit with MDA in terms of the peak position of the FSDP (Fig. S10). Yet, the FSDP of the transition state is broader compared to MDA and displays asymmetry. Overall, on the basis of different phase transitions, thermal stability and diffraction characteristics, MDA is a different material compared to the HDA→LDA transition states.

Using small-angle scattering experiments, HDA itself as well as the HDA→LDA transition states have been suggested to be structurally inhomogenous and contain nanoclusters of different densities(*15*). Our two-dimensional small-angle X-ray scattering (SAXS) data in Fig. S11 shows that MDA displays isotropic scattering which is an important prerequisite for testing its structural homogeneity. The radially integrated SAXS data recorded upon heating MDA is shown in a double-logarithmic plot (Fig. 1H). Following a linear negative decrease, consistent with Porod's law (Fig. S12), a flat region is observed above ~0.3 $Å^{-1}$ for MDA at 100 K. For the vapor-deposited version of LDA, a similar crossover was observed at ~0.5 $Å^{-1}$(*37*). Upon heating, the crossover between the two different scattering regimes shifts towards lower *Q* values. The SAXS intensities at constant *Q* upon heating (Fig. 1I) show small peaks during the MDA to ice I phase transition, which we attribute to the additional scattering contrast as two phases with different densities coexist. The important point is that the scattering intensities change continuously across crystallization implying that the structural origin of the scattering is the same before and after crystallization. After crystallization, the crystalline material is structurally homogeneous implying that the low-*Q* scattering arises solely from surface effects. On the basis of the continuous crossover from MDA to ice I, MDA is therefore also structurally homogeneous as far as its bulk structure is concerned. Furthermore, the scattering intensity levels in the flat scattering regime, which was used as a criterion for structural homogeneity by Koza and coworkers(*15*), are the same within error for MDA and ice I. Overall, the decreases in the low-angle scattering intensities upon heating MDA and ice I are a result of continuous reductions in surface area of otherwise homogeneous materials. Structural heterogeneity is only observed during the MDA→ice I phase transition where two phases of different density coexist within a small temperature window.

We investigated the structural mechanism of the amorphization process through ball milling computationally(*33*). The computational protocol started with a periodically repeated ice I*h* simulation box containing 2880 water molecules that was subjected to random shearing of layers followed by geometry optimization of the local molecular environments (Fig. 2A, Fig. S13). These steps were repeated until the calculated structure factors and other structural characteristics converged (Figs S14-15). The simulations show the evolution of an amorphous fraction (Fig. 2B). We verified the robustness of the computational approach in terms of both path dependence and system size (Figs S16-S17).

During the computational amorphization process, we found a density increase from 0.92 to 0.97 g cm^{-3} (Fig. S19), in line with our experimental observations. The somewhat lower density of the computational MDA compared to the experimental value is attributed to the rigid water molecules in the TIP4P/Ice computer model(*38*) which underestimates the bending of hydrogen bonds in dense structures. Good agreement exists between the calculated and experimental diffraction patterns of MDA in terms of the peak positions of the diffraction features (Fig. 2C). This illustrates that dislocation processes are essential for achieving the amorphization of ice I*h* to the denser MDA. The higher relative peak intensity of the FSDP in the experimental $S(Q)$ with respect to the second peak at ~3 $Å^{-1}$ indicates somewhat more pronounced intermediate-range structural order within the experimental sample compared to the computational structure. The computational recipe for making MDA involves shearing along random directions resulting in a maximally disordered amorphous structure. However, the experimental situation may be slightly different because shearing is likely to proceed at least initially along the characteristic cleavage planes of the crystal leading to a somewhat more ordered amorphous structure. The computational amorphization process goes along with a partial collapse of the second coordination shell of the water molecules (Fig. 2D). This means that water molecules that are not directly hydrogen bonded move towards the first coordination shell which is a well-known structural mechanism for achieving higher densities in ice(*1, 39*).

Interestingly, the computational structure of MDA is closer to liquid water than to LDA. This observation can be seen from the positions of the FSDPs, which are indicators for the intermediate-range structure (Fig. 2C). The FSDPs of MDA and liquid water are found at similar positions whereas the FSDP of LDA is close to ice I*h*. Fig S20 shows a comparison of the experimental positions of the FSDPs of water and the various amorphous ices as a function of temperature including a possible extrapolation from MDA to water. From the oxygen-oxygen pair-distribution functions (Fig. 2D), we observed a progressive collapse of the second coordination shell upon going from ice I*h* to LDA, to MDA, and to liquid water. The same progression can also be seen in the statistics of the primitive ring sizes (Fig. 2E).

The experimental identification of MDA shows that the polyamorphism of H_2O, the existence of multiple distinct amorphous states, is more complex than previously appreciated. A key question is whether MDA should be regarded as a glassy state of liquid water. The glassy natures of LDA and HDA are still debated and a range of different scenarios is possible with the discovery of MDA ice. One interesting possibility is that MDA represents the glass of liquid water, which would be supported by the similar densities and diffraction characteristics(*40*). This would not necessarily violate the well-known liquid-liquid critical point hypothesis(*16, 17, 20, 24, 26*), but MDA would need to have a glass transition temperature above the liquid-liquid critical point. Accordingly, MDA would represent liquid water before the phase separation into LDA and HDA takes place at temperatures below the liquid-liquid critical point. Consistent with this scenario, MDA does not show a glass transition below the recrystallization temperature at ~150 K despite extensive annealing at a range of different temperatures (Fig. S21). Accordingly, MDA would be metastable with respect to either LDA or HDA at low temperatures and at all pressures.

Alternatively, a pressure range might exist at low temperatures within which MDA is more stable than LDA and HDA. However, due to the generally slow kinetics at low temperatures, the two scenarios are difficult to distinguish. Heating MDA at ambient pressure does not lead to the formation of LDA (Fig. 1C) and MDA remained stable upon heating to

the *p*/*T* conditions of eHDA (Fig. S22). The uniaxial compression of MDA at 77 K on the other hand shows a transition to HDA with a step-wise change in volume at an onset pressure of about 1.1 GPa (Fig. 3A). Consistent with the higher density of MDA compared to ice I*h*, the step-wise change in volume is smaller compared to the corresponding transition of the same amount of ice I*h*. The onset pressure of the MDA to HDA transition upon compression is at higher pressures than the LDA to HDA transition found at about 0.5 GPa(*41*).

A third scenario is that MDA is not a glassy liquid but a heavily sheared crystalline state that lacks a connection with the liquid phase. Whatever the precise structural nature of MDA is, we expected it to play a role in the geology of ice at low temperatures, for example, in the many ice moons of the Solar system and beyond. Tidal forces in the interiors of ice moons induced by the gravitational forces of gas giants may cause similar shear forces as found in ball milling and could therefore facilitate the transition of ice I*h* to MDA, provided these occur across a similar temperature and pressure range.

Finally, we note that MDA displays one remarkable property that is not found for any of the other amorphous or crystalline forms of ice. The X-ray diffraction patterns (Fig. 3B) show that the structure of MDA remains unchanged upon compression at 77 K up to 1.0 GPa. Yet, the area of the recrystallization exotherm upon heating at ambient pressure increases substantially from –1.21 ± 0.15 kJ mol^{-1} (SD, *N*=3) for the uncompressed material to –4.02 ± 0.14 kJ mol^{-1} (SD, *N*=3) after compression to 0.5 GPa. Compression to 1.0 GPa leads to a further small increase to –4.17 ± 0.16 kJ mol^{-1} (SD, *N*=3). This value is an extraordinarily large amount of heat that corresponds to about 70% of the heat released upon freezing liquid water to ice I*h*. Because MDA is prepared through ball milling, the amorphous sample is expected to display a high surface area. Given that the X-ray diffraction data remains unchanged upon compression, the increase in the recrystallization enthalpy can be rationalized by the formation of pressure-induced strain at the grain boundaries as has been observed for ball-milled metals(*42*). Similar processes could potentially take place in the ice layers of moons as they are subjected to tidal forces. If this is the case, heat released from the recrystallization of MDA could play a role in activating tectonic motions.

The identification of MDA shows that H_2O is more complex at low temperatures than previously appreciated. The possibility that MDA may represent the true glass of liquid water is an exciting prospect with far reaching consequences for our understanding of liquid water and its many anomalies. Even if it is not, any valid model of water should be able to explain the existence of MDA and its relationship with LDA and HDA. Regardless of the exact nature of MDA, the material has the potential to store mechanical energy from compression, which can be released upon warming at low pressure.

Figures

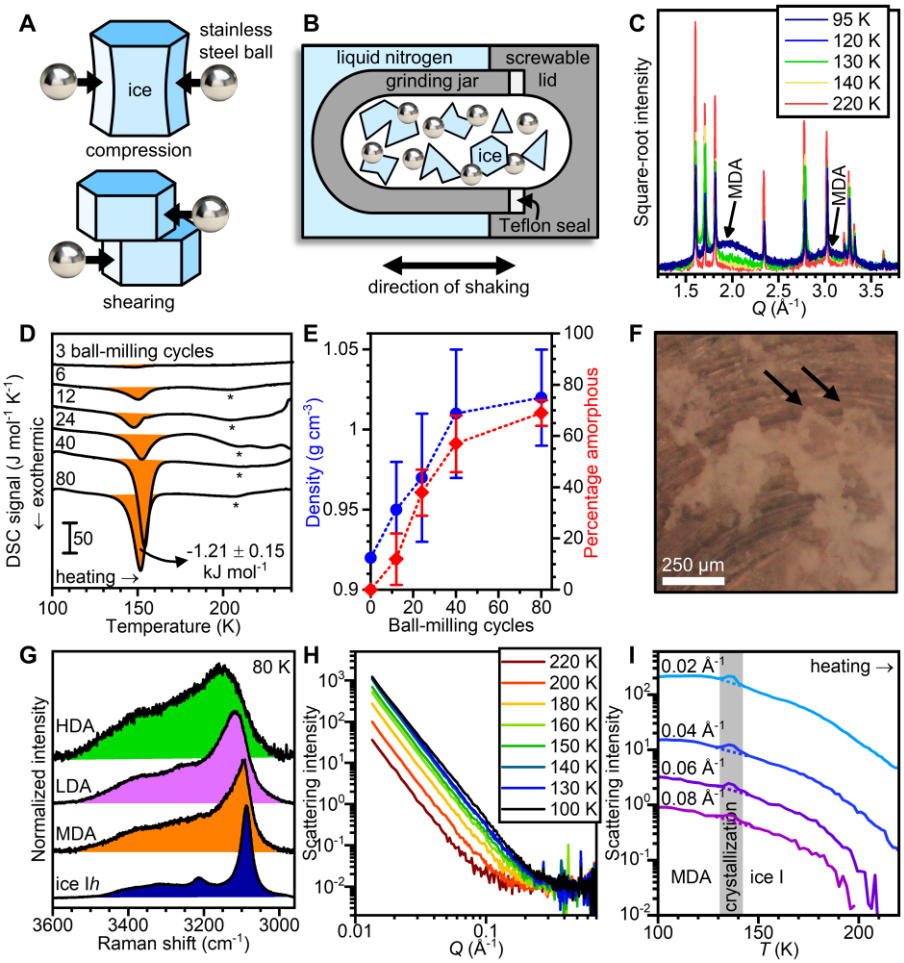

Fig. 1. Preparation and physical properties of medium-density amorphous ice (MDA). (**A**) Illustration of the ball-crystal-ball impact events upon ball milling. (**B**) Schematic of the low-temperature ball-milling setup. (**C**) X-ray diffraction patterns (square-root intensities) upon heating MDA after 80 ball-milling cycles. (**D**) Differential scanning calorimetry of ice ball-milled for increasing numbers of ball-milling cycles. Asterisks mark weak exotherms from the ice I*sd* to ice I*h* phase transitions. (**E**) Density (blue circles) and percentage amorphous content (red diamonds) at 77 K as a function of the ball-milling cycles. Data are mean ± standard deviation and $N \geq 3$. **(F)** Optical microscopy image of MDA powder pressed against a copper substrate. Arrows indicate transparent crystalline ice I*h* impurities. Circular features are part of the substrate. (**G**) Comparison of the Raman spectra of HDA, LDA, MDA and ice I*h* at 80 K in the O-H stretching spectral region. **(H)** Small angle X-ray scattering data of MDA upon heating from 100 to 220 K. **(I)** Scattering intensities at constant Q values as a function of temperature. Dashed lines illustrate continuous intensity changes across crystallization.

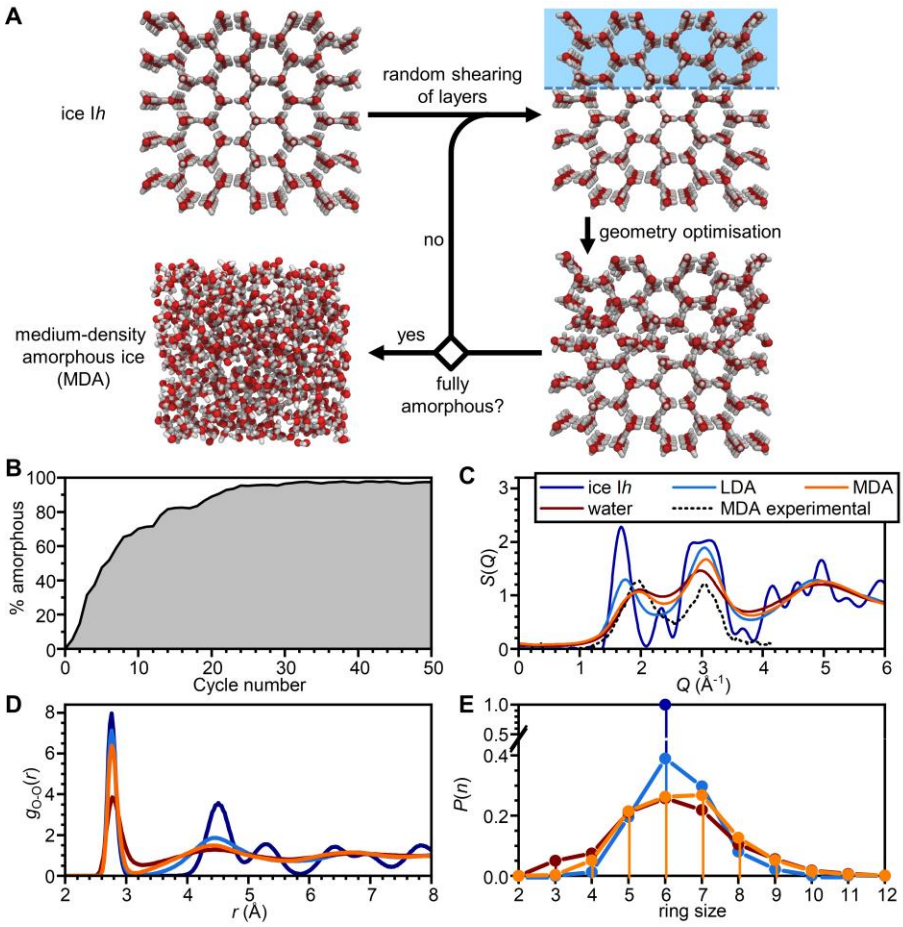

Fig. 2. Computational investigation into the mechanism of formation of MDA. (**A**) Schematic of the computational protocol that yields MDA upon repeated shearing and geometry-optimization steps. **(B)** Percentage amorphous with increasing computational cycles using the local structural analysis shown in Fig. S18. (**C**) Experimental and computational X-ray structure factors, $S(Q)$, of MDA, water, LDA and ice I*h*. (**D**) Corresponding oxygen-oxygen pair distributions functions, $g_{O\text{-}O}(r)$, and (**E**) primitive ring-size distributions. All simulations were carried out using periodic boxes with approximate dimensions of 4.5 nm in *x*, *y* and *z*.

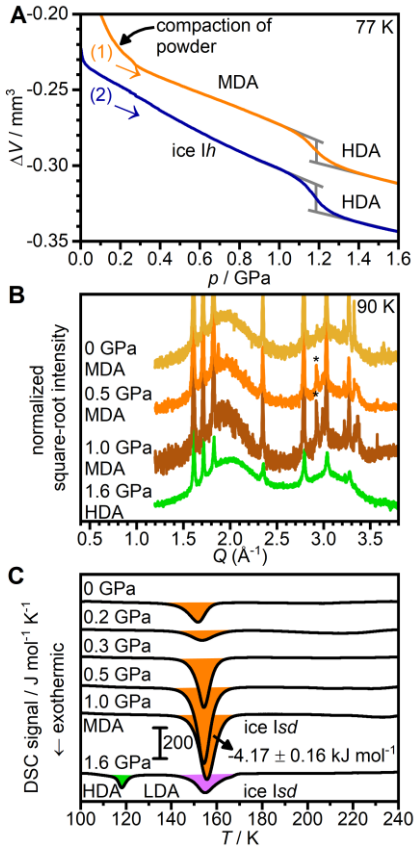

Fig. 3. Effect of pressure on MDA. (**A**) In-situ volume changes upon compression of equal amounts of MDA and ice I*h* to 1.6 GPa at 77 K. Grey lines indicate the step-wise volume changes during the transition to HDA. (**B**) X-ray diffraction patterns at 90 K and ambient pressure after compression of MDA to the indicated pressures at 77 K. (**C**) Differential scanning calorimetry (DSC) scans upon heating at 10 K min^{-1} at ambient pressure after compression of MDA at 77 K. The X-ray diffraction patterns and DSC scans after compression to 1.6 GPa correspond to HDA.

References

1. C. G. Salzmann, Advances in the Experimental Exploration of Water's Phase Diagram. *J. Chem. Phys.* **150**, 060901 (2019).
2. M. Millot, F. Coppari, J. R. Rygg, A. Correa Barrios, S. Hamel, D. C. Swift, J. H. Eggert, Nanosecond X-ray Diffraction of Shock-compressed Superionic Water Ice. *Nature* **569**, 251-255 (2019).
3. R. Yamane, K. Komatsu, J. Gouchi, Y. Uwatoko, S. Machida, T. Hattori, H. Ito, H. Kagi, Experimental evidence for the existence of a second partially-ordered phase of ice VI. *Nat. Comm.* **12**, 1129 (2021).
4. C. G. Salzmann, J. S. Loveday, A. Rosu-Finsen, C. L. Bull, Structure and nature of ice XIX. *Nat. Comm.* **12**, 3162 (2021).
5. T. M. Gasser, A. V. Thoeny, A. D. Fortes, T. Loerting, Structural characterization of ice XIX as the second polymorph related to ice VI. *Nat. Comm.* **12**, 1128 (2021).
6. V. B. Prakapenka, N. Holtgrewe, S. S. Lobanov, A. F. Goncharov, Structure and properties of two superionic ice phases. *Nat. Phys.* **17**, 1233-1238 (2021).
7. T. Loerting, K. Winkel, M. Seidl, M. Bauer, C. Mitterdorfer, P. H. Handle, C. G. Salzmann, E. Mayer, J. L. Finney, D. T. Bowron, How Many Amorphous Ices Are There? *Phys. Chem. Chem. Phys.* **13**, 8783-8794 (2011).
8. E. F. Burton, W. F. Oliver, The Crystal Structure of Ice at Low Temperatures. *Proc. R. Soc. London, Ser. A* **153**, 166-172 (1935).
9. O. Mishima, L. D. Calvert, E. Whalley, 'Melting Ice' I at 77 K and 10 kbar: A New Method of Making Amorphous Solids. *Nature* **310**, 393-395 (1984).
10. O. Mishima, L. D. Calvert, E. Whalley, An Apparently First-order Transition Between Two Amorphous Phases of Ice Induced by Pressure. *Nature* **314**, 76-78 (1985).
11. R. J. Nelmes, J. S. Loveday, T. Strässle, C. L. Bull, M. Guthrie, G. Hamel, S. Klotz, Annealed High-density Amorphous Ice Under Pressure. *Nat. Phys.* **2**, 414-418 (2006).
12. T. Loerting, C. Salzmann, I. Kohl, E. Mayer, A. Hallbrucker, A Second Distinct Structural "State" of High-density Amorphous Ice at 77 K and 1 bar. *Phys. Chem. Chem. Phys.* **3**, 5355-5357 (2001).
13. C. A. Tulk, C. J. Benmore, J. Urquidi, D. D. Klug, J. Neuefeind, B. Tomberli, P. A. Egelstaff, Structural Studies of Several Distinct Metastable Forms of Amorphous Ice. *Science* **297**, 1320-1323 (2002).
14. O. Mishima, Y. Suzuki, Propagation of the polyamorphic transition of ice and the liquid-liquid critical point. *Nature* **419**, 599-603 (2002).
15. M. M. Koza, R. P. May, H. Schober, On the heterogeneous character of water's amorphous polymorphism. *J. Appl. Cryst.* **40**, s517-s521 (2007).
16. P. H. Poole, F. Sciortino, U. Essmann, H. E. Stanley, Phase Behavior of Supercooled Water. *Nature* **360**, 324-328 (1992).
17. O. Mishima, H. E. Stanley, Decompression-induced melting of ice IV and the liquid-liquid transition in water. *Nature* **392**, 164-168 (1998).
18. J. S. Tse, D. D. Klug, C. A. Tulk, I. Swainson, E. C. Svensson, C.-K. Loong, V. Shpakov, V. R. Belosludov, R. V. Belosludov, Y. Kawazoe, The Mechanisms for Pressure-induced Amorphization of Ice Ih. *Nature* **400**, 647-649 (1999).
19. H. Schober, M. M. Koza, A. Tölle, C. Masciovecchio, F. Sette, F. Fujara, Crystal-like High Frequency Phonons in the Amorphous Phases of Solid Water. *Phys. Rev. Lett.* **85**, 4100-4103 (2000).

20. P. G. Debenedetti, Supercooled and glassy water. *J. Phys.: Condens. Matter* **15**, R1669–R1726 (2003).
21. B. Geil, M. M. Koza, F. Fujara, H. Schober, F. Natali, Absence of Fast Precursor Dynamics of Low-density Amorphous Ice around its Hypothetical Glass Transition Temperature. *Phys. Chem. Chem. Phys.* **6**, 677-679 (2004).
22. D. T. Limmer, D. Chandler, Theory of Amorphous Ices. *Proc. Natl. Acad. Sci. USA* **111**, 9413-9418 (2014).
23. J. J. Shephard, S. Ling, G. C. Sosso, A. Michaelides, B. Slater, C. G. Salzmann, Is High-Density Amorphous Ice Simply a "Derailed" State along the Ice I to Ice IV Pathway? *J. Phys. Chem. Lett.* **8**, 1645-1650 (2017).
24. P. G. Debenedetti, F. Sciortino, G. H. Zerze, Second critical point in two realistic models of water. *Science* **369**, 289-292 (2020).
25. C. A. Tulk, J. J. Molaison, A. R. Makhluf, C. E. Manning, D. D. Klug, Absence of amorphous forms when ice is compressed at low temperature. *Nature* **569**, 542-545 (2019).
26. K. H. Kim, K. Amann-Winkel, N. Giovambattista, A. Späh, F. Perakis, H. Pathak, M. L. Parada, C. Yang, D. Mariedahl, T. Eklund, T. J. Lane, S. You, S. Jeong, M. Weston, J. H. Lee, I. Eom, M. Kim, J. Park, S. H. Chun, P. H. Poole, A. Nilsson, Experimental observation of the liquid-liquid transition in bulk supercooled water under pressure. *Science* **370**, 978-982 (2020).
27. S. Kwok, *Physics and Chemistry of the Interstellar Medium*. (University Science Books, Sausalito, USA, 2007).
28. P. Baláž, M. Achimovičová, M. Baláž, P. Billik, Z. Cherkezova-Zheleva, J. M. Criado, F. Delogu, E. Dutková, E. Gaffet, F. J. Gotor, R. Kumar, I. Mitov, T. Rojac, M. Senna, A. Streletskii, K. Wieczorek-Ciurowa, Hallmarks of mechanochemistry: from nanoparticles to technology. *Chem. Soc. Rev.* **42**, 7571-7637 (2013).
29. A. W. Weeber, H. Bakker, Amorphization by ball milling. A review. *Physica B Condens. Matter* **153**, 93-135 (1988).
30. M. Descamps, J. F. Willart, Perspectives on the amorphisation/milling relationship in pharmaceutical materials. *Adv. Drug Deliv. Rev.* **100**, 51-66 (2016).
31. F. Delogu, G. Cocco, Weakness of the "hot spots" approach to the kinetics of mechanically induced phase transformations. *J. Alloys Compd.* **465**, 540-546 (2008).
32. M. Descamps, J. F. Willart, E. Dudognon, V. Caron, Transformation of Pharmaceutical Compounds upon Milling and Comilling: The Role of T_g. *J. Pharm. Sci.* **96**, 1398-1407 (2007).
33. Materials and methods are available as Supplementary Materials on Science Online.
34. T. L. Malkin, B. J. Murray, C. G. Salzmann, V. Molinero, S. J. Pickering, T. F. Whale, Stacking Disorder in Ice I. *Phys. Chem. Chem. Phys.* **17**, 60-76 (2015).
35. F. Perakis, K. Amann-Winkel, F. Lehmkühler, M. Sprung, D. Mariedahl, J. A. Sellberg, H. Pathak, A. Späh, F. Cavalca, D. Schlesinger, A. Ricci, A. Jain, B. Massani, F. Aubree, C. J. Benmore, T. Loerting, G. Grübel, L. G. M. Pettersson, A. Nilsson, Diffusive dynamics during the high-to-low density transition in amorphous ice. *Proc. Natl. Acad. Sci. USA* **114**, 8193-8198 (2017).
36. D. Mariedahl, F. Perakis, A. Späh, H. Pathak, K. H. Kim, C. Benmore, A. Nilsson, K. Amann-Winkel, X-ray studies of the transformation from high- to low-density amorphous water. *Philos. Trans. Royal Soc. A* **377**, 20180164 (2019).

37. C. Mitterdorfer, M. Bauer, T. G. A. Youngs, D. T. Bowron, C. R. Hill, H. J. Fraser, J. L. Finney, T. Loerting, Small-angle neutron scattering study of micropore collapse in amorphous solid water. *Physical Chemistry Chemical Physics* **16**, 16013-16020 (2014).
38. J. L. F. Abascal, E. Sanz, R. García Fernández, C. Vega, A potential model for the study of ices and amorphous water: TIP4P/Ice. *J. Chem. Phys.* **122**, 234511 (2005).
39. J. L. Finney, A. Hallbrucker, I. Kohl, A. K. Soper, D. T. Bowron, Structures of High and Low Density Amorphous Ice by Neutron Diffraction. *Phys. Rev. Lett.* **88**, 22503-22501 (2002).
40. N. Esmaeildoost, H. N. Pathak, A. Späh, T. J. Lane, K. H. Kim, C. Yang, K. Amann-Winkel, M. Ladd-Parada, F. Perakis, J. Koliyadu, A. R. Oggenfuss, P. Johnson, Y. Deng, S. Zerdane, R. Mankowsky, P. Beaud, L. Henrik, A. Nilsson, J. A. Sellberg, Anomalous temperature dependence of the experimental x-ray structure factor of supercooled water. *J. Chem. Phys.* **155**, 214501 (2021).
41. O. Mishima, Reversible First-order Transition between Two H_2O Amorphs at 0.2 GPa and 135 K. *J. Chem. Phys.* **100**, 5910-5912 (1994).
42. H. Gleiter, Nanocrystalline materials. *Prog. Mater. Sci.* **33**, 223-315 (1989).

Acknowledgments: We thank M. Vickers for help with the X-ray diffraction measurements, J. K. Cockcroft for access to a Cryojet, Z. X. Guo for making a cryomill available, and Gabriele Sosso, Martin Fitzner, Andrew Goodwin and the late Paul F. McMillan for discussions. The authors also acknowledge the use of the UCL Kathleen High Performance Computing Facility (Kathleen@UCL) and associated support services as well as the EPSRC CNIE research facility service at University College London for SAXS data collection.

Funding:

European Research Council (ERC) under the European Union's Horizon 2020 research innovation programme grant 725271 (ARF, CGS)

Austrian Science Funds (FWF) grant J4325 (AA)

Materials Chemistry Consortium grant EP/L000202 (MBD, AM)

UK Materials and Molecular Modelling Hub grants EP/P020194/1 and EP/T022213/1 (MBD, AM)

Engineering and Physical Sciences Research Council (EPSRC) grant EP/S03305X/1 (HW)

Author contributions:

Conceptualization: CGS, AS

Investigation: ARF, MBD, AA, HW

Formal Analysis: ARF, CGS, MBD, AM

Funding acquisition: CGS, AM

Software: MBD

Visualization: ARF, CGS, MBD

Writing – original draft: CGS

Writing – review & editing: ARF, MBD, AA, HW, AS, AM, CGS

Competing interests: Authors declare that they have no competing interests.

Data and materials availability: All data needed to evaluate the conclusions in the paper are present in the paper and/or the Supplementary Materials. Experimental data is archived at the Dryad Digital Repository (doi:10.5061/dryad.7sqv9s4wk). Computer code and computational data are available at doi:10.17863/CAM.78718.

Supplementary Materials

Materials and Methods

Figs. S1 to S22

Captions for Movies S1 to S2

Movies S1 to S2